Publications

5-1-2018

Godunov-Type Upwind Flux Schemes of the Two-Dimensional Finite Volume Discrete Boltzmann Method

Leitao Chen
Rice University, chenl12@erau.edu

Laura Schaefer
Rice University

Follow this and additional works at: https://commons.erau.edu/publication

Part of the Fluid Dynamics Commons, Numerical Analysis and Computation Commons, and the Partial Differential Equations Commons

Scholarly Commons Citation

Godunov-type upwind flux schemes of the two-dimensional finite volume discrete Boltzmann method

Leitao Chen and Laura Schaefer

Department of Mechanical Engineering, Rice University, Houston, Texas 77005, USA

Abstract: A simple unified Godunov-type upwind approach that does not need Riemann solvers for the flux calculation is developed for the finite volume discrete Boltzmann method (FVDBM) on an unstructured cell-centered triangular mesh. With piecewise-constant (PC), piecewise-linear (PL) and piecewise-parabolic (PP) reconstructions, three Godunov-type upwind flux schemes with different orders of accuracy are subsequently derived. After developing both a semi-implicit time marching scheme tailored for the developed flux schemes, and a versatile boundary treatment that is compatible with all of the flux schemes presented in this paper, numerical tests are conducted on spatial accuracy for several single-phase flow problems. Four major conclusions can be made. First, the Godunov-type schemes display higher spatial accuracy than the non-Godunov ones as the result of a more advanced treatment of the advection. Second, the PL and PP schemes are much more accurate than the PC scheme for velocity solutions. Third, there exists a threshold spatial resolution below which the PL scheme is better than the PP scheme and above which the PP scheme becomes more accurate. Fourth, besides increasing spatial resolution, increasing temporal resolution can also improve the accuracy in space for the PL and PP schemes.

Keywords: lattice Boltzmann method; discrete Boltzmann method; finite volume method; Godunov flux; unstructured mesh; boundary condition

1. Introduction

The conventional lattice Boltzmann method (LBM) solves the lattice Boltzmann equation (LBE) in a Lagrangian space by coupling the discretization of the particle velocity space and configuration space. With such a coupling mechanism, the Courant-Friedrichs-Lewy (CFL) number can be chosen to be exactly one globally, which means that after each streaming step, the particle distribution functions (PDFs) along all lattice velocities will stop perfectly at grid points. Such a unique feature allows the LBM to achieve second-order accuracy in space with a first-order advection scheme. However, it is this same feature that makes the LBM suffer from several pitfalls, one of which is that the LBM cannot perfectly capture curved boundaries due to its uniform mesh structure [1]. Some pioneering work [2-5] showed that the LBE can simply be considered a special finite-difference version of the more generalized discrete Boltzmann equation (DBE) that is Eulerian in nature. Therefore, one can completely avoid the velocity-configuration coupling by solving the DBE instead of the LBE, which subsequently enables the use of an arbitrary mesh. Following this idea, many Eulerian discrete Boltzmann methods (DBM) have been developed to incorporate complex geometries. Among these, the finite volume discrete Boltzmann method (FVDBM) [6-22] has received the most attention due to the built-in conservative property of the finite volume method (FVM).

Nevertheless, a considerable diffusion error has been, expectedly, observed when the DBE is solved, and especially on irregular grids [6, 23]. Such an error exclusively comes from the evaluation of the advection in Eulerian space. First, the CFL=1 condition will be lost when the DBE is solved in Eulerian space. Numerical viscosity has to be introduced by upwind schemes (or a combination of the upwind scheme and others) to maintain stability [24]. The second reason, which is not unique to the DBE, is that the complex topology on an unstructured mesh will inevitably introduce some error to the advection stencil, part of which eventually becomes numerical viscosity. These explain why, in a previous study, a theoretically second-order scheme for advection could only deliver a result that is slightly higher than first order [25]. As a result, the DBE approaches have an edge over LBE approaches, which is the ability to handle complex geometries with unstructured mesh. However, the consequence for this advantage is a significant increase in numerical error. Therefore, there is a need for higher-order schemes of advection in order to use the DBM as a better alternative to the LBM [26].

The DBE is a hyperbolic equation with a strong advection term. Solving a hyperbolic equation, e.g. the Euler equation or Navier-Stokes (NS) equation, with minimum diffusion error while maintaining stability is a constant concern in the computational fluid dynamics (CFD) community. After decades of development, there are many successful techniques, among which Godunov's method has dominated many CFD codes in the subgenre of FVM, due to its higher fidelity and better stability. In Godunov's method, the advected scalar is considered as a wave moving at its characteristic velocity. Then, a Riemann problem appears at the interface between two adjacent cells, which is solved by exact or approximate Riemann solvers, e.g. Roe's solver [27]. Different reconstructions of the wave structure determine the order of Godunov's method. The piecewise-constant (PC) reconstruction proposed in the original work from Godunov [28], the piecewise-linear (PL) method developed by Van Leer [29-33] that gave birth to the still popular Monotone Upstream Scheme for Conservation Laws (MUSCL), and the piecewise-parabolic (PP) reconstruction introduced by Colella and Woodward [34, 35] give the first-order, second-order and third-order Godunov's method, respectively.

Despite the high success of Godunov's method in the CFD community, its importance is not recognized widely within the LBM circle. Most FVDBM [6-18, 22] work treats the advected scalar in the advection term as a scalar value in a static point of view, in contrast to Godunov's method. The only application of Godunov's method in FVDBM so far was employed by Patil and Lakshmisha in their simulations of single-phase problems [19-21], which involve a Riemann solver and a limiter that satisfies the Total Variation Diminishing (TVD) property. However, the linear advection term in the DBE (i.e. the advection has a constant speed that is defined by the lattice velocity) and the mutual independence among all PDFs do not require any type of Riemann solver when calculating the PDF flux on the face between two neighbor cells (this will be explained in detail later in this paper). The TVD limiters, which were originally developed for simulating one-dimensional (1D) shocks in CFD tools, were first introduced into LBM simulations by Teng et al. [36] and Lee et al. [37] to solve the streaming step of LBE for multi-phase problems that experience sharp gradients similar to acoustic shocks. Therefore, TVD limiters are not necessary when the flows are single-phase and do not have large gradients if simulated by the DBE. More importantly, it was pointed out very early in the CFD community by Goodman and LeVeque that TVD limiters are no better than first-order accurate when extended to multiple dimensions [38]. This is probably why only an

overall first-order accuracy in space was reported for their flux scheme with TVD limiters in the work of Patil and Lakshmisha [19-21].

Therefore, in order to achieve better accuracy in space, a simple Godunov-type upwind approach that does not require any Riemann solver for the advection of FVDBM is developed in the present paper. Then, with different PDF wave reconstructions (PC, PL and PP) on a universal stencil, three Godunov flux schemes with different orders of accuracy are formulated. After that, a semi-implicit temporal scheme specifically designed for the presented Godunov-type flux scheme is shown. In order to make comparisons between the Godunov and non-Godunov schemes, a standard second-order upwind (SOU) scheme, which is non-Godunov, and the corresponding time-marching approach are also provided. Next, a boundary treatment that works seamlessly with all of the developed flux schemes is also established. With thorough numerical testing, some important conclusions can be reached.

2. Formulation of the FVDBM

The DBE with the Bhatnagar-Gross-Krook (BGK) collision model, which is obtained by discretizing the particle velocity space of the continuous Boltzmann equation with a finite number of velocity components [39], is shown as follows:

$$\frac{\partial f_\alpha}{\partial t} + \boldsymbol{e}_\alpha \cdot \boldsymbol{\nabla} f_\alpha = -\frac{1}{\tau}\left(f_\alpha - f_\alpha^{eq}\right) \qquad \alpha = 0,1,2,\dots,M-1 \tag{1}$$

where f and f^{eq} are the PDF and equilibrium PDF respectively, and $\boldsymbol{e}$ is the lattice velocity. The subscript α indicates the αth member out of M total components of the discretized particle velocity space, and τ is the relaxation time. By choosing a proper lattice model, $\boldsymbol{e}_\alpha$ and f_α^{eq} can be defined explicitly. For example, for the commonly used D2Q9 lattice, they are defined as:

$$\boldsymbol{e}_\alpha = \begin{cases} [0,0]c & \alpha = 0 \\ \left[cos\left((\alpha-1)\frac{\pi}{2}\right), sin\left((\alpha-1)\frac{\pi}{2}\right)\right]c & \alpha = 1-4 \\ \left[cos\left((\alpha-5)\frac{\pi}{2}+\frac{\pi}{4}\right), sin\left((\alpha-5)\frac{\pi}{2}+\frac{\pi}{4}\right)\right]\sqrt{2}c & \alpha = 5-8 \end{cases} \tag{2}$$

$$f_\alpha^{eq} = \omega_\alpha \rho \left[1 + \frac{\boldsymbol{e}_\alpha \cdot \boldsymbol{u}}{c_s^2} + \frac{(\boldsymbol{e}_\alpha \cdot \boldsymbol{u})^2}{2c_s^4} - \frac{\boldsymbol{u} \cdot \boldsymbol{u}}{2c_s^2}\right] \tag{3}$$

$$\omega_\alpha = \begin{cases} \frac{4}{9} & \alpha = 0 \\ \frac{1}{9} & \alpha = 1-4 \\ \frac{1}{36} & \alpha = 5-8 \end{cases} \tag{4}$$

where c is the constant lattice speed for isothermal flow and is usually chosen to be unity, and c_s is the speed of sound. For D2Q9:

$$c_s^2 = c^2/3 \tag{5}$$

The relation between relaxation time and flow viscosity is defined as:

$$\nu = \tau c_s^2 \tag{6}$$

In Eq. (3), ρ and $\boldsymbol{u}$ are the macroscopic flow variables that are recovered from the PDFs as follows:

$$\begin{bmatrix} \rho \\ \boldsymbol{u} \end{bmatrix} = \Sigma_{\alpha=0}^{M-1} \begin{bmatrix} f_\alpha \\ \boldsymbol{e}_\alpha f_\alpha \end{bmatrix} \tag{7}$$

In order to solve Eq. (1) in a FVM fashion, the configuration space needs to be discretized, from which the control volume (CV) shall be created. In the present paper, the triangular mesh is selected due to its excellent adaptability to complex boundaries and its simple geometric structure. Then the CV is chosen to be the triangle itself, with point P as the centroid. The solution is chosen to be stored and updated at P. Hereafter, unless stated otherwise, the centroid is used to represent the CV (e.g., the CV P has its centroid at P). Taking the integral of Eq. (1) over the triangular CV and moving the gradient term to the right hand side:

$$\int_{CV} \frac{\partial f_\alpha}{\partial t} dA = \int_{CV} \frac{1}{\tau} (f_\alpha^{eq} - f_\alpha) dA - \int_{CV} \boldsymbol{e}_\alpha \cdot \boldsymbol{\nabla} f_\alpha dA \tag{8}$$

The first and second terms are simple integrals and can be simplified with the cell-averaged values as:

$$\int_{CV} \frac{\partial f_\alpha}{\partial t} dA = \frac{\partial \bar{f}_\alpha}{\partial t} A_{CV} \tag{9}$$

$$\int_{CV} \frac{1}{\tau} (f_\alpha^{eq} - f_\alpha) dA = \frac{1}{\tau} (\bar{f}_\alpha^{eq} - \bar{f}_\alpha) A_{CV} \tag{10}$$

where A_{CV} is the area of the CV. Since P is the centroid, here it is assumed that the value at the centroid is equal to the cell-averaged value, so:

$$\bar{f}_\alpha = f_\alpha(P) \tag{11}$$

$$\bar{f}_\alpha^{eq} = f_\alpha^{eq}(P) \tag{12}$$

Then, equations (9) and (10) can be rewritten as

$$\int_{CV} \frac{\partial f_\alpha}{\partial t} dA = \frac{\partial \bar{f}_\alpha}{\partial t} A_{CV} = \frac{\partial f_\alpha(P)}{\partial t} A_{CV} \tag{13}$$

$$\int_{CV} \frac{1}{\tau} (f_\alpha^{eq} - f_\alpha) dA = \frac{1}{\tau} (\bar{f}_\alpha^{eq} - \bar{f}_\alpha) A_{CV} = \frac{1}{\tau} [f_\alpha^{eq}(P) - f_\alpha(P)] A_{CV} \tag{14}$$

The gradient term in integral form in Eq. (8) is the net flux of the PDF through the boundaries of the CV according to the Gauss divergence theorem. Therefore:

$$\int_{CV} \boldsymbol{e}_\alpha \cdot \boldsymbol{\nabla} f_\alpha dA \ = \ \sum_{i=1}^{3} F_{\alpha,i} \tag{15}$$

where $F_{\alpha,i}$ is the PDF flux on ith face of the triangular CV.

As a result, the finite volume form of the DBE is:

$$T_\alpha \ = \ C_\alpha - F_\alpha \tag{16}$$

where T_α, C_α and F_α are the temporal term, collision term and flux term respectively, as follows:

$$T_\alpha = \frac{\partial f_\alpha(P)}{\partial t} \tag{17}$$

$$C_\alpha = \frac{1}{\tau}\left[f_\alpha^{eq}(P) - f_\alpha(P)\right] \tag{18}$$

$$F_\alpha = \frac{1}{A_{CV}} \sum_{i=1}^{3} F_{\alpha,i} \tag{19}$$

The collision term is the simplest one to calculate since it is localized, and is neither derivative nor integral. The temporal term is treated with a special time-marching scheme, which will be discussed in a later section. The flux term F_α is the most difficult to calculate, and will be developed and discussed in the following sections.

3. Godunov Flux Schemes

3.1. A Universal Stencil and Flux Schemes Overview

Since the flux calculations on all faces of the CV are identical, the subscript i for the face index can be omitted in the following equation:

$$F_\alpha = \widetilde{f}_\alpha (\boldsymbol{e}_\alpha \cdot \boldsymbol{n})L \tag{20}$$

where $\widetilde{f}_\alpha$ is the average PDF on the face, $\boldsymbol{e}_\alpha$ is the lattice velocity, $\boldsymbol{n}$ is the face unit normal, and L is the length of the face. In Eq. (20), the only unknown is $\widetilde{f}_\alpha$, which can be calculated with a variety of methods. In this paper, those methods for $\widetilde{f}_\alpha$ are called flux schemes, although they do not directly calculate the fluxes of PDFs.

The flux schemes require a stencil that can provide geometric (length, distance, etc.) and solution (the PDFs at the centroids of nearby CVs) information. Since only the flux that has the same direction as the face normal is effective, and the PDFs are highly direction-dependent (each f_α has its own advection velocity vector $\boldsymbol{e}_\alpha$), the stencil in this paper is constructed in such a way that it is orthogonal to the face

and passes the geometric center of the face. Figure 1 shows the stencil line (the dashed line) of the face of interest, V_1V_2 whose center point is C. It can be assumed that:

$$\widetilde{f_\alpha} = f_\alpha(C) \tag{21}$$

In order to have a high-order flux scheme in space, the stencil to be constructed should be sufficiently long. In addition, since the lattice velocity $\boldsymbol{e}_\alpha$ spans a 2π direction when α changes from 0 to $M-1$, the stencil has to be symmetric with respect to the face center, point C. Consequently, a stencil consisting of four points, P', Q', R', and S' (two on each side of the center point), is constructed. P', Q', R', and S' are the feet of the centroids P, Q, R, and S onto the stencil line. The CVs P and Q are readily available since they are immediately attached to the face V_1V_2. However, there are multiple choices for R and S, because there are many centroids whose feet have longer distances to the face center than P and Q. Two simple conditions are devised to rule out others and make sure there is only one R and S. Condition one is that the foot of the centroid has to be located within its own CV, and condition two is if multiple centroids satisfy condition one, choose the centroid whose foot is closest to the face center. For example, in Fig. 1, centroid T_1 is not selected because T_1' is located outside of its own CV; S is chosen over T_2 since S' is closer to C than T_2'.
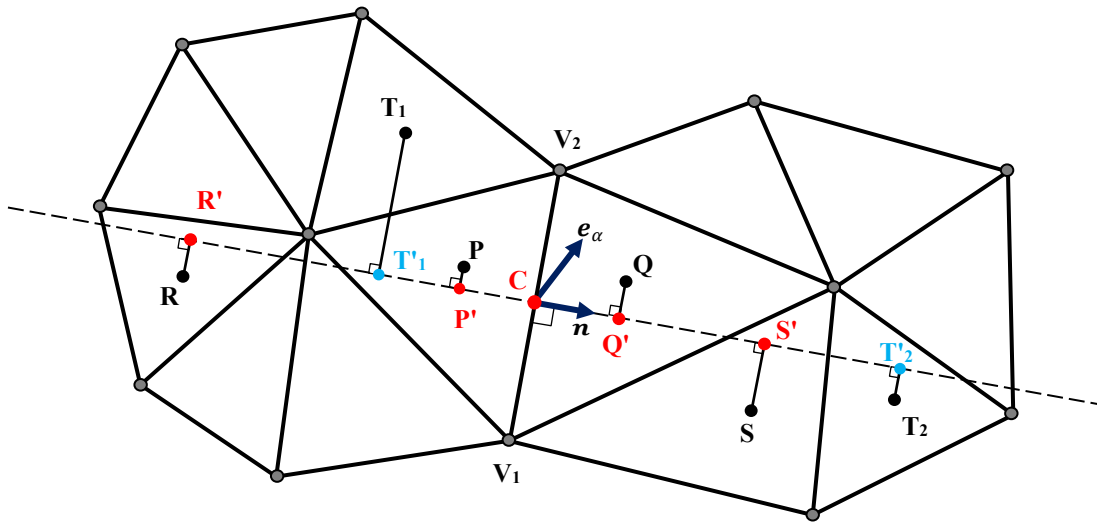

Figure 1. A universal stencil for flux calculation

With the help of the stencil in Fig.1, the original two-dimensional (2D) problem is transformed into a local 1D problem. By considering the direction of $\boldsymbol{e}_\alpha$, the four-point stencil in Fig. 1 is further developed to an $\boldsymbol{e}_\alpha$-dependent three-point stencil, as shown in Fig. 2.

u_α

UU   U   C   D

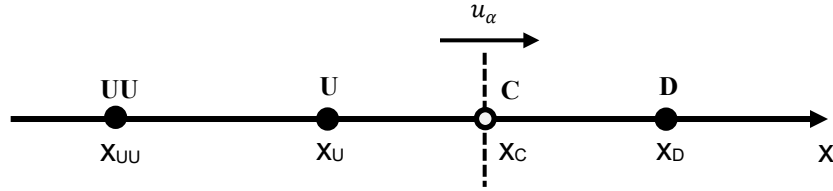x_{UU} x_U x_C x_D X

Figure 2. Lattice velocity-dependent three-point stencil across the face of interest

In Fig. 2, point C is the same C in Fig. 1. The positivity of the axis is defined by the lattice velocity $\boldsymbol{e}_\alpha$, not the face normal $\boldsymbol{n}$. As a result, D, U, and UU denote the downwind, upwind, and further upwind stencil points, with respect to the speed u_α:

$$u_\alpha = |\boldsymbol{e}_\alpha \cdot \boldsymbol{n}| \tag{22}$$

The mapping between the three-point and four-point stencils is defined as follows, based on the direction of $\boldsymbol{e}_\alpha$:

$$\begin{cases} f_\alpha(D) = f_\alpha(Q'), & f_\alpha(U) = f_\alpha(P'), & f_\alpha(UU) = f_\alpha(R') \quad for \ (\boldsymbol{e}_\alpha \cdot \boldsymbol{n}) > 0 \\ f_\alpha(D) = f_\alpha(P'), & f_\alpha(U) = f_\alpha(Q'), & f_\alpha(UU) = f_\alpha(S') \quad for \ (\boldsymbol{e}_\alpha \cdot \boldsymbol{n}) \leq 0 \end{cases} \tag{23}$$

Accordingly, the geometric relations are defined as:

$$\begin{cases} \begin{aligned} L_D &= |x_c - x_D| = |\boldsymbol{x}_c - \boldsymbol{x}_{Q'}|, & L_U &= |x_c - x_U| = |\boldsymbol{x}_c - \boldsymbol{x}_{P'}|, \\ L_{UU} &= |x_c - x_{UU}| = |\boldsymbol{x}_c - \boldsymbol{x}_{R'}| & & for \ (\boldsymbol{e}_\alpha \cdot \boldsymbol{n}) > 0 \\ L_D &= |x_c - x_D| = |\boldsymbol{x}_c - \boldsymbol{x}_{P'}|, & L_U &= |x_c - x_U| = |\boldsymbol{x}_c - \boldsymbol{x}_{Q'}|, \\ L_{UU} &= |x_c - x_{UU}| = |\boldsymbol{x}_c - \boldsymbol{x}_{S'}| & & for \ (\boldsymbol{e}_\alpha \cdot \boldsymbol{n}) \leq 0 \end{aligned} \end{cases} \tag{24}$$

where L_D, L_U, and L_{UU} are the distances from the face center C to the downwind point D, upwind point U, and further upwind point UU, respectively. Figure 2 has one less stencil point than Fig. 1 because flux schemes generally do not use the further downwind point.

With the transformation from Fig. 1 to Fig. 2, the flux scheme can be put in a general formula that calculates $f_\alpha(C)$ as a function of $f_\alpha(D)$, $f_\alpha(U)$, and $f_\alpha(UU)$, and other grouped variables $\mathcal{H}$, namely:

$$f_\alpha(C) = \Psi[f_\alpha(D), f_\alpha(U), f_\alpha(UU), \mathcal{H}] \tag{25}$$

The theoretical order of accuracy of any flux scheme is directly related to the number of active stencil points in this formula. Equation (25) is theoretically third-order in space. If only a subset of $\Omega \in \{f_\alpha(D), f_\alpha(U), f_\alpha(UU)\}$ is utilized, the theoretical order of the scheme will become lower. Generally speaking, Eq. (25) is theoretically second-order if $|\Omega| = 2$ and first-order if $|\Omega| = 1$. The actual order of accuracy of any flux scheme will be lower than its theoretical order. It is important to emphasize that no matter what flux scheme is applied, it has to be used on all PDFs (α ranges from 0 to $M - 1$). For example,

if the D2Q9 lattice is selected, Eq. (25) has to be executed nine times for each face. Therefore, the computing overhead of the overall model is largely dominated by Eq. (25).

The nature of Godunov flux schemes and their fundamental differences from the non-Godunov counterparts are depicted in Fig. 3. For non-Godunov schemes (Fig. 3(a)), at any time step, t_n, the profile of the PDF (the solid curved line) can be assumed along the stencil. Then, the PDF at the face center can be geometrically interpolated or extrapolated using the profile at t_n. For Godunov schemes (Fig. 3(b)), the same profile is constructed at t_n. However, such a profile is treated as a wave moving at speed u_α. At t_{n+1}, the wave has traveled a distance (the dashed curve line). So, between t_n and t_{n+1}, $f_\alpha(C)$ is not a constant value but changing from $f_\alpha{}^n(C)$ to $f_\alpha{}^{n+1}(C)$. In essence, the non-Godunov schemes statically use the PDF profile at a given moment; while the Godunov schemes take the course of movement of the PDF profile for a period of time into account. Due to this more advanced treatment, the Godunov schemes have become a dominant method for solving hyperbolic problems.
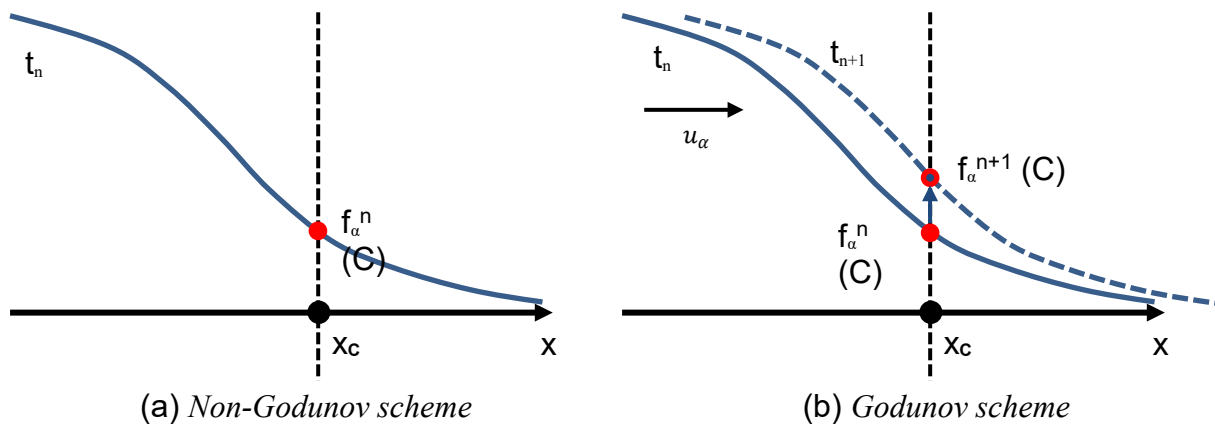

Figure 3. Difference between Godunov and non-Godunov flux schemes

The next task is to substantiate Eq. (25) into explicit forms, which will be discussed in Sec. 3.2. Before doing that, the PDFs at stencil points, $f_\alpha(P')$, $f_\alpha(Q')$, $f_\alpha(R')$, and $f_\alpha(S')$ need to be evaluated. Otherwise, Eq. (23) cannot be closed. In Fig. 1, the stencil points P', Q', R', and S' are generally not the solution points (the centroids). Therefore, the PDFs at the stencil points are unknown, and they need to be guessed. It can be seen that any other points on the stencil line have longer distances to the centroids than their feet, the stencil points. Therefore, it can be safely assumed that:

$$f_\alpha(P') = f_\alpha(P), \qquad f_\alpha(Q') = f_\alpha(Q), \qquad f_\alpha(R') = f_\alpha(R), \qquad f_\alpha(S') = f_\alpha(S) \qquad (26)$$

Eq. (26) is only a first-order approximation in space by assuming the PDFs within each CV are constant. Higher-order approximations will improve the solution accuracy. But they are not covered in this paper since they are not flux schemes.

3.2 Godunov flux schemes in explicit forms

The typical Godunov scheme in a CFD application requires a Riemann solver, since the hyperbolic equation to be solved (Euler or NS) has a nonlinear advection term, and the advection is coupled with acoustics. Therefore, the matrix for the advection will have two or more real eigenvalues, each of which determines a wave speed. Such a phenomenon with two wave speeds is illustrated in Fig. 4, in which the advected scalar λ has an initial profile at t_n across the face center, as in Fig. 4(a). Such a profile will move simultaneously to the left and right with different speeds u_1 and u_2. At time t_{n+1}, the value of λ at the face center is determined by overlapping two waves, as shown in Fig. 4(b). In order to solve the overlapped waves, a Riemann solver is the best choice. However, a Riemann solver is not needed for the gradient term in the DBE, $\boldsymbol{e}_\alpha \cdot \boldsymbol{\nabla} f_\alpha$, for two reasons. First, the advection is linear, since $\boldsymbol{e}_\alpha$ is constant once the lattice model is determined. Second, all PDFs are mutually independent. Essentially, each PDF f_α exclusively has its own advection speed $\boldsymbol{e}_\alpha$. Due to these two unique properties, when projected on the stencil, the matrix of each advected scalar, f_α, has one and only one real eigenvalue, $|\boldsymbol{e}_\alpha \cdot \boldsymbol{n}|$. As a result, a Riemann solver, such as Roe's solver used in work of Patil and Lakshmisha [19-21] is a more complex technique than what is required.
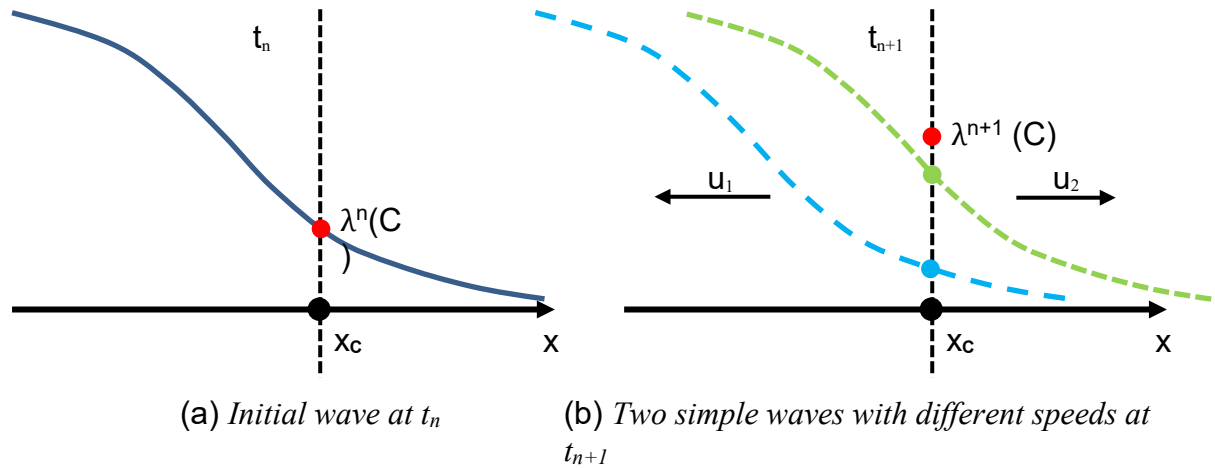

(a) *Initial wave at t_n*   (b) *Two simple waves with different speeds at t_{n+1}*

Figure 4. Wave propagation with two speeds

Instead, a simple integral over time can suffice [41]. Assuming that the PDF at face center is the average value over the course of the wave movement from t_n to t_{n+1}, then:

$$f_\alpha{}^{[n,n+1]}(C) = \frac{1}{\Delta t} \int_{t_n}^{t_{n+1}} f_\alpha(x_c, t)\, dt \tag{27}$$

where the notation [n,n+1] in the superscript indicates it is a time averaged value from t_n to t_{n+1}. Since $f_\alpha(x_c, t)$ is a simple wave with only a positive wave speed, u_α (Eq. (22)), and since $f_\alpha(x_c, t)$ does not change its shape during its propagation, Eq. (27) is equivalent to:

$$f_\alpha{}^{[n,n+1]}(C) = \frac{1}{\Delta t} \int_{t_n}^{t_{n+1}} f_\alpha(x_c, t)\, dt = \frac{1}{\Delta t} \int_{t_n}^{t_{n+1}} f_\alpha(x_c - u_\alpha(t - t_n), t_n)\, dt \tag{28}$$

With the variable transformation $x = x_c - u_\alpha(t - t_n)$, then $dt = -dx/u_\alpha$. Therefore, Eq. (28) becomes:

$$f_\alpha^{[n,n+1]}(C) = \frac{1}{u_\alpha \Delta t} \int_{x_1}^{x_2} f_\alpha(x, t_n)\, dx \tag{29}$$

where:

$$x_1 = x|_{t=t_{n+1}} = x_c - u_\alpha \Delta t \tag{30}$$

$$x_2 = x|_{t=t_n} = x_c \tag{31}$$

And $\Delta t = (x_2 - x_1)/u_\alpha$. In addition, $f_\alpha(x, t_n)$ becomes $f_\alpha^n(x)$ with a simpler notation. Finally, the Godunov flux scheme becomes:

$$f_\alpha^{[n,n+1]}(C) = \frac{1}{x_2 - x_1} \int_{x_1}^{x_2} f_\alpha^n(x)\, dx \tag{32}$$

Equation (32) is the general form of the Godunov-type flux schemes. The original temporal integral is transformed into a spatial integral whose physical meaning is illustrated in Fig. 5. It can be seen that the Godunov-type flux is the average height of the shaded area from x_1 to x_2 under the PDF profile curve at time step t_n.
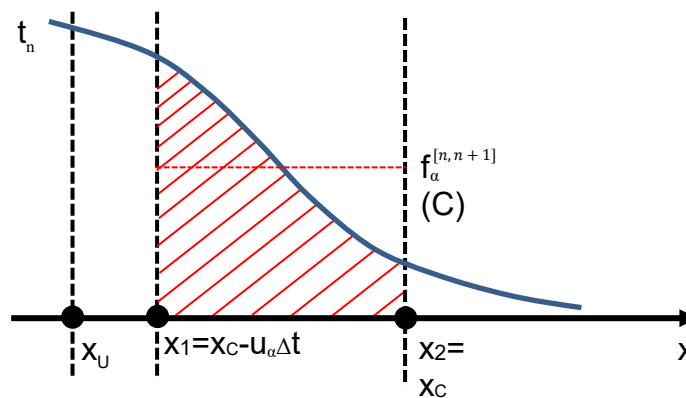
Figure 5. Figurative representation of the general form of the Godunov flux schemes

The scheme developed here is upwind in nature since the shaded region is always located to the left of the face center. Therefore, it is named the Godunov-type upwind flux scheme. Due to this upwind feature, the CFL condition can also be developed. Since the left bound of the shaded region x_1 cannot exceed the upwind stencil point x_U, therefore:

$$\frac{u_\alpha \Delta t}{L_U} \leq 1 \tag{33}$$

Equation (33) is the local CFL condition. However u_α and L_U differ from location to location. In order to maintain a global stability of Eq. (32), Eq. (33) should be modified as:

$$\frac{(u_\alpha)_{max}\Delta t}{(L_U)_{min}} \leq 1 \tag{34}$$

It is necessary to know the definition of the PDF profile (the curved line in Fig. 5) to calculate the integral, Eq. (32). The actual profile cannot be obtained, but can be reconstructed with a piecewise-constant (PC), piecewise-linear (PL), or piecewise-parabolic (PP) assumption. Therefore, different Godunov-type upwind flux schemes with different orders of accuracy can be developed. Due to the upwind nature of the developed scheme, the PC, PL, and PP reconstruction only need to hold in the region to the left of the face center ($x \leq x_c$).

For the PC reconstruction, as shown in Fig. 6(a), Eq. (32) reduces to:

$$f_\alpha^{[n,n+1]}(C) = \frac{1}{x_2 - x_1} f_\alpha^n(U)(x_2 - x_1) = f_\alpha^n(U) \tag{35}$$

which is exactly the standard first-order upwind scheme (FOU) that is also non-Godunov (because it only uses the PDF profile at t_n), and is theoretically first-order in space.

For PL (Fig. 6(b)), a linear profile passing through $f_\alpha^n(C)$ and $f_\alpha^n(U)$ is reconstructed. The general formula for the linear profile is $f_\alpha^n(x) = c_1 x + c_2$. Therefore, Eq. (32) becomes:

$$f_\alpha^{[n,n+1]}(C) = \frac{1}{2}c_1(x_1 + x_2) + c_2 \tag{36}$$

where:

$$c_1 = \frac{f_\alpha^n(C) - f_\alpha^n(U)}{x_C - x_U} \tag{37}$$

$$c_2 = f_\alpha^n(U) - \frac{x_U}{x_C - x_U}[f_\alpha^n(C) - f_\alpha^n(U)] \tag{38}$$

Combining Eqs. (36), (37) and (38), and using Eqs. (30) and (31) to replace x_1 and x_2, then:

$$f_\alpha^{[n,n+1]}(C) = f_\alpha^n(U) + \left(1 - \frac{u_\alpha \Delta t}{2L_U}\right)[f_\alpha^n(C) - f_\alpha^n(U)] \tag{39}$$

where $f_\alpha^n(C)$ is linearly interpolated between $f_\alpha^n(D)$ and $f_\alpha^n(U)$, as shown in Fig. 6(b), as:

$$f_\alpha^n(C) = \frac{L_U}{L_D + L_U} f_\alpha^n(D) + \frac{L_D}{L_D + L_U} f_\alpha^n(U) \tag{40}$$

Eq. (39) is the final explicit form of the PL Godunov-type upwind flux scheme, which is theoretically second-order in space. Equation (39) is numerically the same as the Lax-Wendroff scheme discussed in one of our previous studies [25], due to Eq. (40).

For the PP reconstruction (Fig. 6(c)), its general form is $f_\alpha^n(x) = c_1 x^2 + c_2 x + c_3$, which replaces the integrant in Eq. (32). Then, Eq. (32) becomes:

$$f_\alpha^{[n,n+1]}(C) = \frac{1}{3}c_1 u_\alpha^2 \Delta t^2 - \left(c_1 x_C + \frac{1}{2}c_2\right)u_\alpha \Delta t + c_1 x_C^2 + c_2 x_C + c_3 \tag{41}$$

where c_1, c_2 and c_3 are obtained by the following linear operation:

$$\begin{pmatrix} c_1 \\ c_2 \\ c_3 \end{pmatrix} = \begin{pmatrix} x_C^2 & x_C & 1 \\ x_U^2 & x_U & 1 \\ x_{UU}^2 & x_{UU} & 1 \end{pmatrix}^{-1} \cdot \begin{pmatrix} f_\alpha^n(C) \\ f_\alpha^n(U) \\ f_\alpha^n(UU) \end{pmatrix} \tag{42}$$

and where $f_\alpha^n(C)$ is also obtained by Eq. (40).

If choosing the face center as the origin of the x axis and the positivity of the axis is pointing to the right, namely $x_C=0$ and $x_{UU}<x_U<0$, then Eqs. (41) and (42) become:

$$f_\alpha^{[n,n+1]}(C) = \frac{1}{3}c_1 u_\alpha^2 \Delta t^2 - \frac{1}{2}c_2 u_\alpha \Delta t + c_3 \tag{43}$$

$$\begin{pmatrix} c_1 \\ c_2 \\ c_3 \end{pmatrix} = \begin{pmatrix} 0 & 0 & 1 \\ L_U^2 & -L_U & 1 \\ L_{UU}^2 & -L_{UU} & 1 \end{pmatrix}^{-1} \cdot \begin{pmatrix} f_\alpha^n(C) \\ f_\alpha^n(U) \\ f_\alpha^n(UU) \end{pmatrix}$$

$$= \begin{pmatrix} \dfrac{1}{L_U L_{UU}} & \dfrac{1}{L_U^2 - L_U L_{UU}} & \dfrac{1}{L_{UU}^2 - L_U L_{UU}} \\ \dfrac{L_U + L_{UU}}{L_U L_{UU}} & \dfrac{L_{UU}}{L_U^2 - L_U L_{UU}} & \dfrac{L_U}{L_{UU}^2 - L_U L_{UU}} \\ 1 & 0 & 0 \end{pmatrix} \cdot \begin{pmatrix} f_\alpha^n(C) \\ f_\alpha^n(U) \\ f_\alpha^n(UU) \end{pmatrix} \tag{44}$$

Equations (43) and (44) are the final explicit form of the third-order Godunov-type upwind flux scheme.
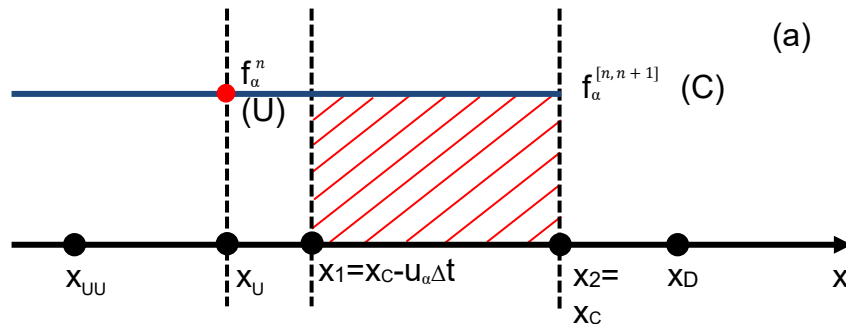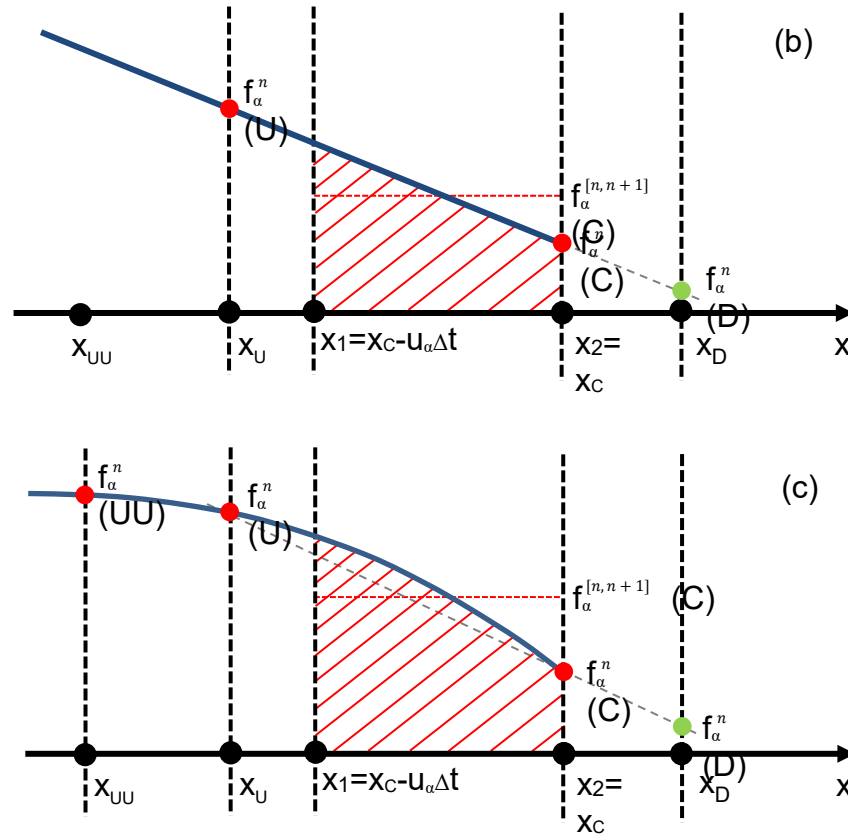
Figure 6. Godunov flux schemes with different wave reconstructions. (a) Piecewise Constant; (b) Piecewise Linear; (c) Piecewise Parabolic

Usually the spatial accuracy can only be changed by changing the spatial resolution. It is interesting to note that the PL (Eq. (39)) and PP (Eq. (43)) schemes are also functions of Δt. Therefore, increasing the temporal resolution, not only the spatial resolution, can also improve the accuracy in space. Such a unique feature is exclusively due to the wave-like treatment of the PDF profile across the face interface and the linear advection in the DBE. By increasing temporal resolution (i.e. decreasing Δt) in Fig. 5 the distance between x1 and x2 becomes shorter. As a result, the PL and PP reconstructions of the profile will be closer to their true values. Consequently, the spatial accuracy can be improved.

However, such an accuracy improvement is limited by a minimum allowable Δt which cannot be decreased infinitely towards zero. Otherwise, the PL and PP schemes will become unstable. For the PL scheme (Eq. (39)), when Δt approaches zero, the term that contains Δt will also approach zero, so that Eq. (39) is equivalent to:

$$f_\alpha^{[n,n+1]}(C) \approx f_\alpha^n(U) + [f_\alpha^n(C) - f_\alpha^n(U)] = f_\alpha^n(C) \tag{45}$$

Since $f_\alpha^n(C)$ is obtained through central differencing, Eq. (40), the PL scheme will become unconditionally unstable. The same thing happens to the PP scheme. When Δt vanishes, the PP scheme (Eqs. (43) and (44)) reads:

$$f_\alpha^{[n,n+1]}(C) \approx c_3 = f_\alpha^n(C) \tag{46}$$

which is the same central differencing. Therefore, the accuracy improvement of the PL and PP schemes by decreasing Δt will be capped by an invisible stability condition. The actual value of minimum Δt may differ from one specific problem to another.

For comparison, with the same stencil (Figs. 1 and 2), a standard second-order upwind scheme (SOU) that is essentially non-Godunov can also be formulated. By using the PDF profile at t_n, the SOU reads:

$$f_\alpha^n(C) = \left(\frac{L_D}{L_D + L_U} + \frac{L_U}{L_D + L_U} \cdot \frac{L_D + L_{UU}}{L_{UU} - L_U} \right) f_\alpha^n(U) - \left(\frac{L_U}{L_{UU} - L_U} \right) f_\alpha^n(UU) \tag{47}$$

By comparing the FOU and SOU with the PL and PP schemes, it can be seen that the non-Godunov schemes are not a function of Δt. Therefore, changing the temporal resolution does not affect the spatial accuracy of the non-Godunov flux schemes.

4. The Time Marching Scheme

Since the Godunov-type flux schemes calculate the PDFs at the face center with a temporal integral from t_n to t_{n+1} (Eq. (27)), the total flux for each CV obtained by Eqs. (20) and (19) is also a value based on a temporal integral from t_n to t_{n+1}. Therefore, Eq. (19) becomes:

$$F_\alpha^{[n,n+1]} = \frac{1}{A_{CV}} \sum_{i=1}^3 F_{\alpha,i}^{[n,n+1]} = \frac{1}{A_{CV}} \sum_{i=1}^3 f_{\alpha,i}^{[n,n+1]}(C)(\boldsymbol{e}_\alpha \cdot \boldsymbol{n}_i) L_i \tag{48}$$

Therefore, when plugging $F_\alpha^{[n,n+1]}$ back into the governing equation Eq. (16), a special time marching scheme is required, in which the other two terms should also be integrated over time from t_n to t_{n+1}. Then, Eq. (16) becomes:

$$T_\alpha^{[n,n+1]} = C_\alpha^{[n,n+1]} - F_\alpha^{[n,n+1]} \tag{49}$$

where:

$$T_\alpha^{[n,n+1]} = \frac{1}{\Delta t} \int_{t_n}^{t_{n+1}} \frac{\partial f_\alpha(P)}{\partial t} \, dt \approx \frac{1}{\Delta t} [f_\alpha^{n+1}(P) - f_\alpha^n(P)] \tag{50}$$

$$C_\alpha^{[n,n+1]} = \frac{1}{\Delta t} \int_{t_n}^{t_{n+1}} \frac{1}{\tau} \left[f_\alpha^{eq}(P) - f_\alpha(P) \right] dt \tag{51}$$

Assuming $f_\alpha^{eq}(P) - f_\alpha(P)$ linearly changes from t_n to t_{n+1}, then Eq. (51) becomes:

$$C_\alpha^{[n,n+1]} = \frac{1}{\tau \Delta t} \frac{\left[f_\alpha^{eq,n+1}(P) - f_\alpha^{n+1}(P) \right] + \left[f_\alpha^{eq,n}(P) - f_\alpha^n(P) \right]}{2} \Delta t \tag{52}$$

Next, Eqs. (50) and (52) can be combined with Eq. (49), which is reduced to become:

$$f_\alpha^{n+1}(P) = \frac{2\tau - \Delta t}{2\tau + \Delta t} f_\alpha^n(P) + \frac{\Delta t}{2\tau + \Delta t} \left[f_\alpha^{eq,n+1}(P) + f_\alpha^{eq,n}(P) \right] - \frac{2\tau \Delta t}{2\tau + \Delta t} F_\alpha^{[n,n+1]} \tag{53}$$

where $f_\alpha^{eq,n+1}(P)$ is linearly extrapolated according to the scheme suggested by Mei and Shyy [40]:

$$f_\alpha^{eq,n+1}(P) = 2f_\alpha^{eq,n}(P) - f_\alpha^{eq,n-1}(P) \tag{54}$$

Equation (53) is semi-implicit. Therefore, it is more stable than explicit schemes such as the Forward Euler and Runge-Kutta methods.

It should be noted that for the non-Godunov approach, since the flux is evaluated at t_n, and not from t_n to t_{n+1}, the time marching of the governing equation (Eq. (16)) that utilizes a non-Godunov flux is different from that for the Godunov flux schemes (Eq. (49)). In order to increase stability, Lee and Lin [50] introduced a semi-implicit scheme that contains an implicit collision, but an explicit advection, to solve the DBE, which could be adopted here. As a result, Eq. (16) for the non-Godunov flux schemes becomes:

$$T_\alpha^n = C_\alpha^{n+1} - F_\alpha^n \tag{55}$$

where F_α^n is the total flux over the entire CV calculated by a non-Godunov flux scheme, such as the SOU in Eq. (47). In addition, with the Forward Euler method:

$$T_\alpha^n = \frac{1}{\Delta t} [f_\alpha^{n+1}(P) - f_\alpha^n(P)] \tag{56}$$

and the implicit collision term:

$$C_\alpha^{n+1} = \frac{1}{\tau} \left[f_\alpha^{eq,n+1}(P) - f_\alpha^{n+1}(P) \right] \tag{57}$$

where $f_\alpha^{eq,n+1}(P)$ is extrapolated in the same way as Eq. (54), the time marching for the non-Godunov flux schemes becomes:

$$f_\alpha^{n+1}(P) = \frac{\tau}{\tau + \Delta t} f_\alpha^n(P) + \frac{\Delta t}{\tau + \Delta t} f_\alpha^{eq,n+1}(P) - \frac{\tau \Delta t}{\tau + \Delta t} F_\alpha^n \tag{58}$$

5. Boundary treatment

The boundary treatment is equally as important as the solution schemes. Without a proper boundary treatment, the flux schemes developed in Sec. 3 cannot be used to solve actual problems. In order to preserve the merits of solving the DBE on an unstructured mesh and the proposed flux scheme, a desirable boundary treatment should satisfy the following requirements:

- It should allow the universal stencil (Fig. 1) and all presented flux schemes to be realized in a unified way on or near the boundaries.
- It should be second-order accurate.
- It should ignore the difference in local mesh topology.

- It should incorporate different lattice models in a unified way.

The boundary treatment developed by Chen and Schaefer [25] can satisfy the above requirements; however, this only works on a two-point stencil and needs to be adapted for the much longer four-point stencil in the present paper. The Chen-Schaefer boundary treatment consists of two steps. First, the stencil is completed by creating a ghost stencil point for the missing one. Second, the boundary nodal PDFs that are obtained by the given physical boundary conditions (velocity and density) are used to evaluate the PDFs at ghost stencil points. The same two-step approach is applied for the current boundary treatment, but with extra developments.

5.1 Construction of ghost stencil points

Some of the stencil points will be missing when the owner face of the stencil is on the boundaries (Fig. 7(a)). Due to the prolonged length of the stencil, even when the owner face is located in the interior but close enough to the boundaries, part of the stencil points may still be missing (Fig. 7(b)).

In Fig. 7(a), on face N_1N_2, its ghost stencil points Q' and S' are constructed such that:

$$|Q'C| = |P'C| \tag{59}$$

and:

$$|Q'S'| = |Q'C| \tag{60}$$

Therefore, the PDFs at Q' and S' can be geometrically extrapolated as:

$$f_\alpha(Q') = 2f_\alpha(C) - f_\alpha(P') \tag{61}$$

$$f_\alpha(S') = 2f_\alpha(Q') - f_\alpha(C) \tag{62}$$

where $f_\alpha(C)$ can be interpolated with the PDFs at boundary nodes N_1 and N_2. Since point C is the face center:

$$f_\alpha(C) = \frac{1}{2}[f_\alpha(N_1) + f_\alpha(N_2)] \tag{63}$$

The problem can be closed if $f_\alpha(N_1)$ and $f_\alpha(N_2)$ are available, which will be introduced in Sec. 5.2. It is worth noting that the PDF construction at the ghost stencil point S' is only needed when the PP or SOU flux scheme is applied (in which the further upwind stencil point $f_\alpha^n(UU)$ is required). Otherwise, if the PL is chosen for the flux calculation, depending on the local lattice velocity, one of $f_\alpha(P')$ and $f_\alpha(Q')$ is $f_\alpha^n(U)$ and the other one is $f_\alpha^n(D)$ in Eqs. (39) and (40). Then, the PDF construction at the ghost stencil point S' can be saved.

In Fig. 7(b), on the interior face N_2N_3, only one stencil point, S', is missing. If the PP or SOU is selected, the PDF construction at the ghost stencil point S' becomes necessary. The stencil line is extended to the

exterior region and is intercepted by the boundary at point I. Similarly, S' is constructed in such a way that:
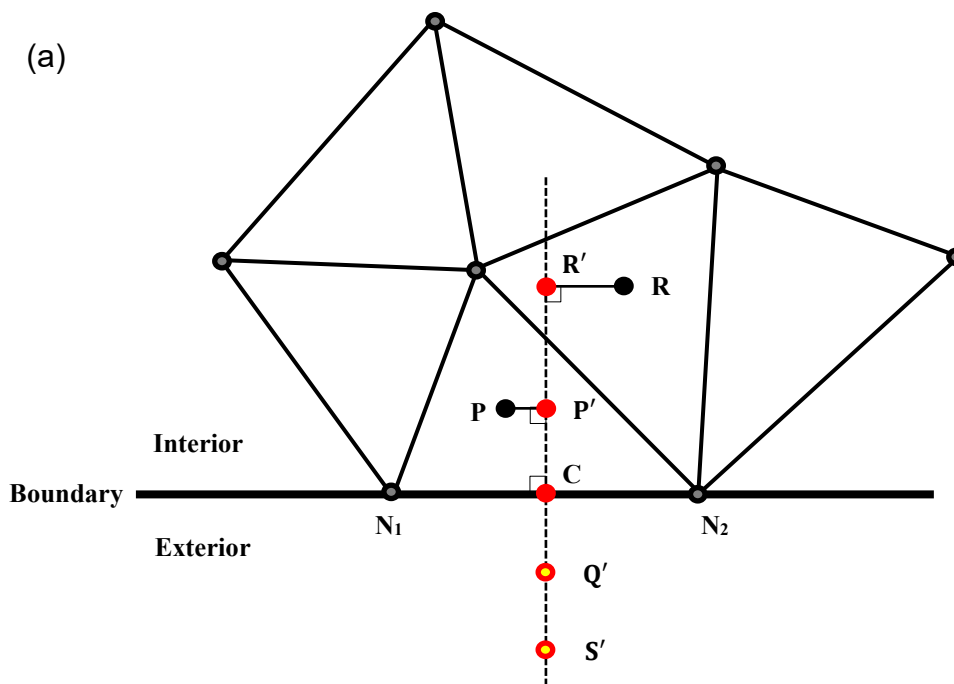
$$|S'I| = |Q'I| \tag{64}$$

Therefore:

$$f_\alpha(S') = 2f_\alpha(I) - f_\alpha(Q') \tag{65}$$

where:

$$f_\alpha(I) = \frac{|N_2I|}{|N_1N_2|}f_\alpha(N_1) + \frac{|N_1I|}{|N_1N_2|}f_\alpha(N_2) \tag{66}$$

Once the stencil is complete, the flux through the owner face is calculated with the same flux schemes as in Sec. 3. Now, the question is how to evaluate the PDFs at boundary nodes N_1 and N_2.

(a)

(b)
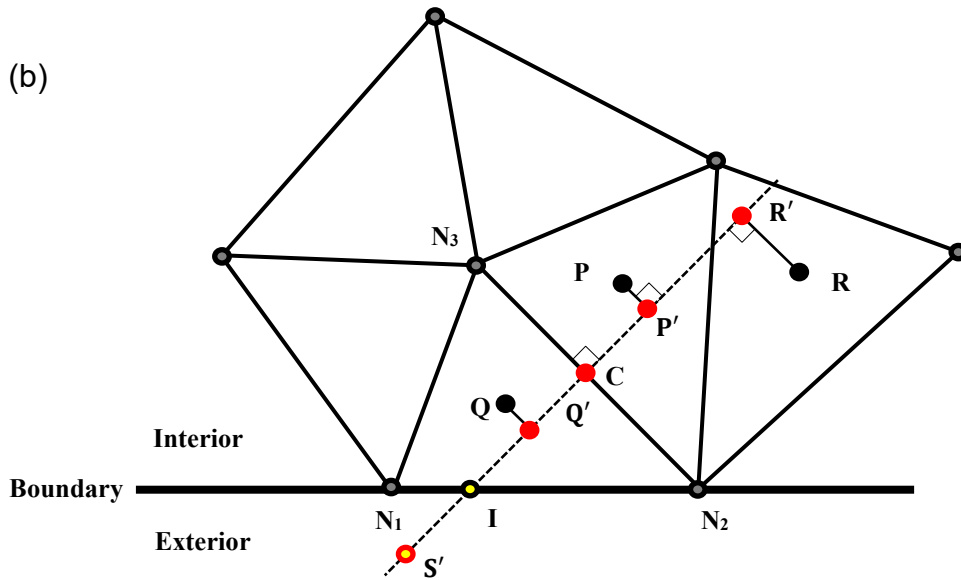
Figure 7. Construction of ghost stencil points. (a) scenario one: the owner face (face N₁N₂) is on the boundary; (b) scenario two: the owner face (face N₂N₃) is not on the boundary

5.2 Evaluation of the boundary nodal PDF

For any boundary node, N, as shown in Fig. 8, it is connected to an arbitrary number of triangular cells. For example, P_1, P_2, P_3, and P_4 are the centroids of all of the triangular cells connected to N, and d_1, d_2, d_3, and d_4 the distances between the corresponding centroids and N.
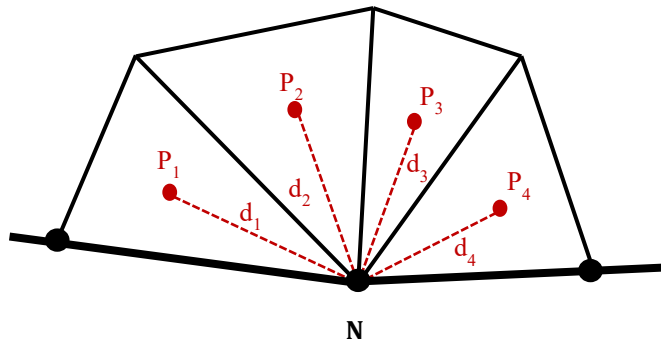
Figure 8. Extrapolation scheme for boundary node

For any variable θ, its value at boundary node N can be extrapolated with a function Υ such that:

$$\theta(N) = \Upsilon\{\theta(P)\} = \frac{\sum_{j=1}^{X} \frac{\theta(P_j)}{d_j}}{\sum_{j=1}^{X} \frac{1}{d_j}} \tag{67}$$

where X is the total number of connected triangular cells. This extrapolation scheme is fully compatible with different boundary geometries and local mesh topology. Instead of manipulating the total PDF at the boundary nodes, here it is chosen to decompose the total PDF into an equilibrium part and non-equilibrium part [42]:

$$f_\alpha(N) = f_\alpha^{eq}(N) + f_\alpha^{neq}(N) \tag{68}$$

The equilibrium part is obtained by using Eqs. (2) - (4), in which ρ and $\boldsymbol{u}$ are the physical boundary conditions. In the cases where only one of ρ and $\boldsymbol{u}$ is known on the boundary, the other variable is extrapolated using Eq. (68), in which θ is replaced by that unknown variable (please refer to [25] for more detail). Therefore, all of the components of the equilibrium PDFs can be computed once no matter what type of lattice model is applied. $f_\alpha^{neq}(N)$ is computed using Eq. (68), in which θ is replaced by f_α^{neq}.

6. Numerical results and discussions

There are two types of meshes used in this paper, which are shown in Fig. 9. The first type of mesh consists of all isosceles right triangles (IRT) with fixed topology and identical size and shape. This type of mesh is not able to capture a curved boundary. The mesh consists of many squared blocks that have four triangles in each of them. For the one shown in Fig. 9 (a), there are nine blocks in each direction, so, it is a 9×9 IRT mesh. The other type of mesh (Fig. 9 (b)) is more general, with random topology and arbitrarily shaped and sized triangles, and therefore can achieve exact body-fitting for complex boundary geometries.
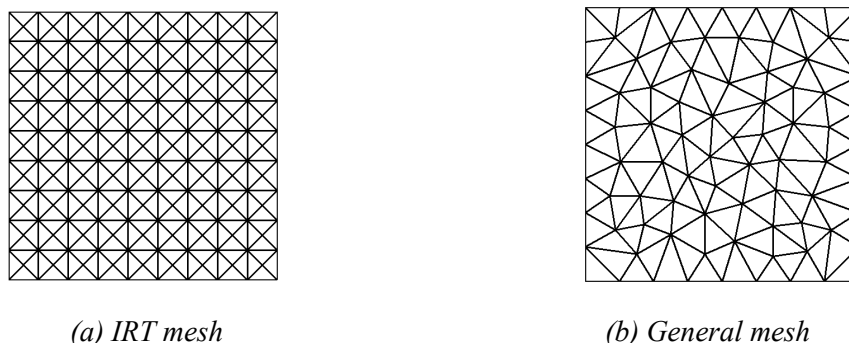

(a) IRT mesh   *(b) General mesh*

Figure 9. Two different types of mesh

The first difference between these two types of meshes is the size and shape of each triangular cell, which can be obviously seen in Fig. 9. The second difference is the local connectivity, or topology, at each node. For the IRT mesh, eight triangular cells share each interior node, and four are connected to each boundary node except for the corner nodes (two triangular cells). For the general mesh, the number of triangular cells connected to each node, no matter where it is located, is arbitrary. Therefore, the IRT mesh is only a special case of the general mesh.

Although the IRT mesh is not as able to capture a curved boundary as the general mesh, it is still necessary in the current study. A mandatory numerical test for any numerical method is to study the errors at different mesh resolution, which is used to characterize the order of accuracy of that numerical method. During the error study, the mesh size is refined by a fixed factor (usually two) several times, and the errors

of the numerical solutions are measured after each refinement. With the general mesh, it is very difficult, if not impossible, to increase the mesh size with a fixed factor. Even though that is achievable, there is no guarantee that the mesh topology after each refinement will be kept the same. Therefore, both types of triangular meshes are used in the current work, where the IRT mesh is used for the spatial error study while the general mesh is used for other numerical cases.

However, both meshes are completely unstructured. On the back end, they have exactly the same data structures and finite volume solution techniques. Therefore, the proposed FVDBM scheme and boundary treatment can solve a problem on any triangular mesh in the same way, including the two types of meshes used in this paper, and other triangular meshes not covered here.

6.1 Taylor-Green vortex flow

In order to quantitatively study the developed flux schemes without the influence of boundary conditions, Taylor-Green vortex (TGV) flow with only periodic boundaries is chosen for the first study case. The analytical solution of the velocity at any location (*x,y*) and any moment *t* is defined as follows:

$$u_a = -u_0 \cos(k_1 x) \sin(k_2 y) \, e^{[-v(k_1^2 + k_2^2)t]} \tag{69}$$

$$v_a = -u_0 \frac{k_1}{k_2} \sin(k_1 x) \cos(k_2 y) \, e^{[-v(k_1^2 + k_2^2)t]} \tag{70}$$

where u_0 is the initial velocity, v is the viscosity, and k_1 and k_2 are two parameters defined as:

$$k_1 = \frac{2\pi}{D_x} \tag{71}$$

$$k_2 = \frac{2\pi}{D_y} \tag{72}$$

where D_x and D_y are the length and the height of the rectangular computational domain.

In order to study the spatial errors of the flux schemes only due to the spatial resolution, the errors contributed by other sources have to be minimized and kept constant, since it is impossible to separate one type of error from another. It is well known that there are two major and unique errors when solving the DBE (and the LBE as well) with BGK collision: the compressibility error that scales with Ma^2 and the BGK truncation error that is proportional to τ^2. In addition, the spatial errors of the developed Godunov-type flux schemes also depend on temporal resolution. Therefore, in the following numerical study, a small u_0 is chosen so that Ma=0.01 for the D2Q9 lattice. The relaxation time is kept small as $\tau = 0.006$, and it is kept that $\Delta t = 0.2\tau$. Three IRT meshes are prepared: 18×18, 36×36, and 72×72, which double the mesh resolution in the *x* and *y* directions each time. The parameter Δx is used here to quantify the mesh resolution, similar to the Cartesian mesh in finite difference methods, and is defined as:

$$\Delta x = \sqrt{2A_{CV}} \tag{73}$$

where A_{CV} is the area of the triangular CV. Since the IRT mesh is applied, A_{CV} is the same for all triangular CVs. TGV flow is a transient problem. The flow has an initial vorticity that decays with time. Therefore, the numerical solution at a certain moment has to be selected. In the current study, the numerical solution is chosen as the moment when the simulated vorticity becomes half of the initial state. The corresponding analytical solution is calculated with Eqs. (69-72) by using the time t of the numerical solution. All developed Godunov-type and non-Godunov flux schemes are tested. Their relative solutions errors in L_2 norm of the x velocities are calculated as follows:

$$Err_u = \frac{\|u_a - u_n\|_2}{\|u_a\|_2} \tag{74}$$

where u_a and u_n are the analytic and numerical solutions, respectively. The error for each flux scheme at each mesh resolution is plotted in Fig. 10.
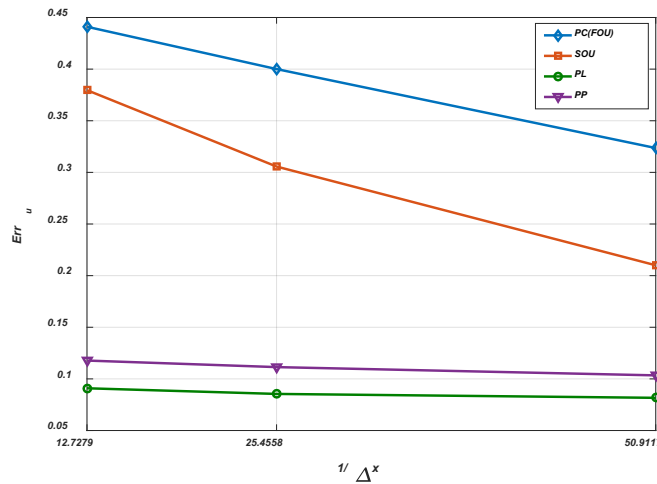
Figure 10. The velocity errors of Taylor-Green vortex flow at different mesh resolutions for different Godunov-type and non-Godunov flux schemes

First, the comparison between SOU and PL (both second-order in theory) shows that the PL scheme is more accurate than the SOU at all tested mesh resolutions, which demonstrates the advantage of Godunov flux schemes over their non-Godunov counterparts. For the DBE, a hyperbolic equation with a strong advection term, treating the propagation of the PDFs as a moving wave in the Godunov-type flux schemes, is more suitable to capture the correct underlying physics than the non-Godunov flux schemes. Second, it can be seen that the PC scheme generates a much higher error than the PL and PP schemes at all tested mesh resolutions. This is one important reason why the PC or FOU scheme is never recommended for simulating advection, let alone the DBE with a strong advection. Second, the PL and PP schemes are very similar in terms of numerical error. However, although PP is theoretically a higher-order scheme than the PL, it does not display a smaller error at all tested mesh resolutions. By observing the error difference between the PP and PL schemes at different mesh resolutions in Fig. 11, it can be seen that their difference in error is monotonically decreasing while increasing the mesh resolution. This indicates that by increasing the mesh resolution, the error of the PP scheme is decreasing faster than the PL scheme, and, more importantly, that decrease is accelerating. The only reason why the PP scheme

generates a larger error than PL in the current test is because the mesh is not fine enough. Therefore, there must exist a pivotal mesh resolution, below which the PL scheme is more accurate and above which the PP scheme is more accurate. The reason why the PP scheme is not more accurate monotonically than the PL scheme is due to interplay of the positive and negative effects of using a longer stencil. As mentioned earlier, a three-point stencil used in the PP scheme provides more information than a two-point stencil in the PL scheme. However, another consequence caused by the extra stencil point is the dramatic change of the shape of the constructed PDF profile, which can be seen in Fig. 6. For the Godunov-type flux schemes, the PDFs at the face center are based on the spatial integral under the profile curve. Therefore, the shape of the PDF profile is critical. A slight change of the profile shape will result in a nontrivial change of the integral under the curve, and consequently the PDF value at the face center. As a result, when the mesh is coarse, the geometric length of the stencil for the PP scheme is very long, and the shape of the PDF profile constructed with such a stencil is less accurate than that from a shorter stencil of the PL scheme. Consequently, the numerical error of the PP scheme with a coarse mesh is larger than for the PL scheme. When the mesh is refined, the stencil will become geometrically shorter. Therefore, the improvement of the profile shape with the three-point stencil of the PP scheme will be more than that with the two-point stencil of the PL scheme, followed by lower numerical error.
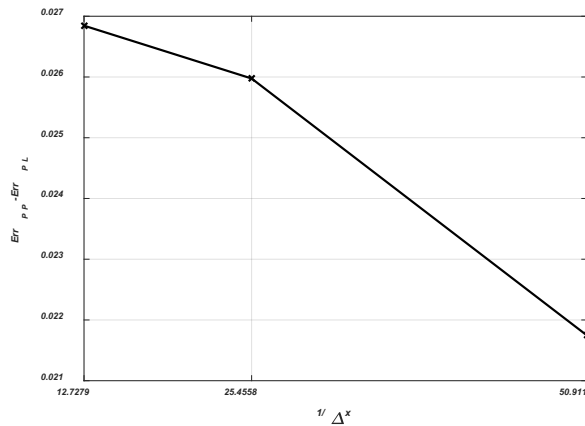

Figure 11. The difference in velocity errors between the PP and PL schemes of Taylor-Green vortex flow at different mesh resolutions

As discussed in Sec 3.2, the spatial error of the Godunov-type flux schemes can also be decreased by increasing the temporal resolution. However, increasing the temporal resolution can also decrease the error for simulating a transient problem with any time marching scheme. Since the TGV flow is transient in nature, when increasing the temporal resolution, it is impossible to separate the gained accuracy of the flux scheme from that of the time marching scheme. As a result, the study of the accuracy of the flux schemes at different temporal resolutions is saved for later cases that have a steady-state solution.

6.2 Couette flow

This flow has a moving wall on the top and a stationary wall at the bottom of the domain. The left and right boundaries are periodic. The analytical solution for the *x* velocity is a linear profile between zero and the moving velocity of the top wall. The moving wall is given a horizontal moving velocity such that the Mach number is *Ma* = 0.01 with a D2Q9 lattice to minimize the compressibility error. The relaxation time is also $\tau = 0.006$ to restrain the BGK truncation error, where $\Delta t = 0.4\tau$. The same set of IRT meshes used in the TGV flow is also adopted here. The relative x velocity error in the L_2 norm (Eq.(74)) at different mesh

resolutions for different flux schemes are plotted in Fig. 12. It can be seen that at the lowest mesh resolutions where *1/dx*=12.7279, PC is the most accurate and PP is the least accurate. However, at the highest mesh resolution where *1/dx*=50.9117, PP is the most accurate while PC is the least accurate. The decrease in error while increasing mesh resolution becomes gradually faster from PC to PL to PP since the theoretical order of accuracy increases from PC to PL to PP. However, it is worth noting that at the lowest mesh resolution the PL and PP schemes generate more error than the PC scheme. On the contrary, in the TGV flow, at any mesh resolution, the PL and PP schemes have smaller errors than the PC scheme. The difference in this observation may lie in the physical difference between the TGV flow and Couette flow. The former is highly non-linear and its solution is strongly depending on viscosity, while the latter one is linear and its solution is viscosity-independent. One major type of error that is reduced by using a higher-order flux scheme is the numerical viscosity. When modeling Couette flow at low mesh resolutions, the viscosity-independent solution cannot benefit from the reduced numerical viscosity by using higher-order flux schemes. As a result, the total reduced amount of all other types of errors cannot offset the negative effects of the longer stencil when using higher-order methods. Therefore, at the lower mesh resolutions, using a higher-order flux scheme will adversely increase the numerical error. Due to the same negative effects of using a longer stencil for a viscosity-independent problem, the SOU that has a very long stencil due to the utilization of the further upwind stencil point UU (Eq. (47)) displays a counterintuitively larger error than the FOU at all tested mesh resolutions. Based on these observations, and continuing to compare the SOU with the PL and PP in Fig. 12, it is easy to conclude, again, that the Godunov flux schemes are more accurate than the non-Godunov ones, here for the viscosity-independent flows.

When comparing PL and PP in particular, one can see that the error of PP becomes less than that of PL at the mesh resolution *1/dx*=25.4558, which means that pivotal mesh resolution is between 12.7279 and 25.4558. However, for the TGV flow, such a pivotal mesh resolution is beyond *1/dx*=50.9117 (See in Fig. 11). This indicates that for different flow problems the pivotal mesh resolution bears different values.
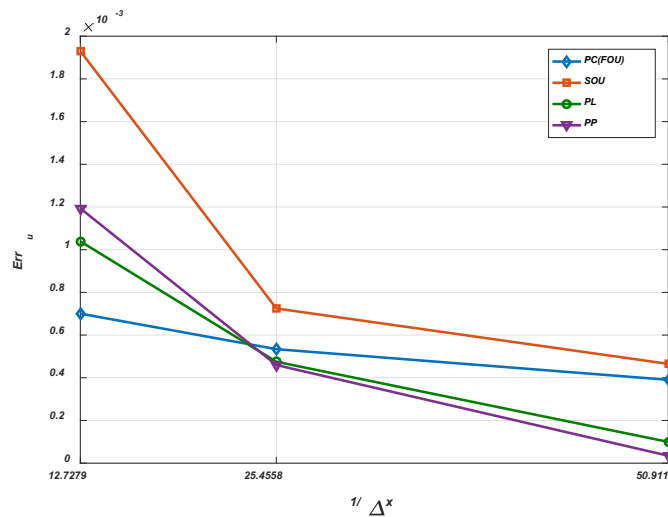

Figure 12. The velocity errors of Couette flow at different mesh resolutions for different Godunov-type and non-Godunov flux schemes

Since Couette flow has a steady-state solution, it can be used to study the spatial error at different temporal resolutions. Here four values are chosen, $\Delta t/\tau = 0.8, 0.4, 0.2, 0.1$ for the same 36*36 IRT mesh. The relative *x* velocity error in the L_2 norm at different temporal resolutions for different flux schemes are plotted in Fig. 13. It can be seen that the error of the PC(FOU) and SOU schemes are constant at different

temporal resolution simply because their formulations are not a function of Δt. On the contrary, the errors of the PL and PP schemes monotonically decrease with the increasing of temporal resolution. This is the second advantage of Godunov flux schemes over the non-Godunov ones.
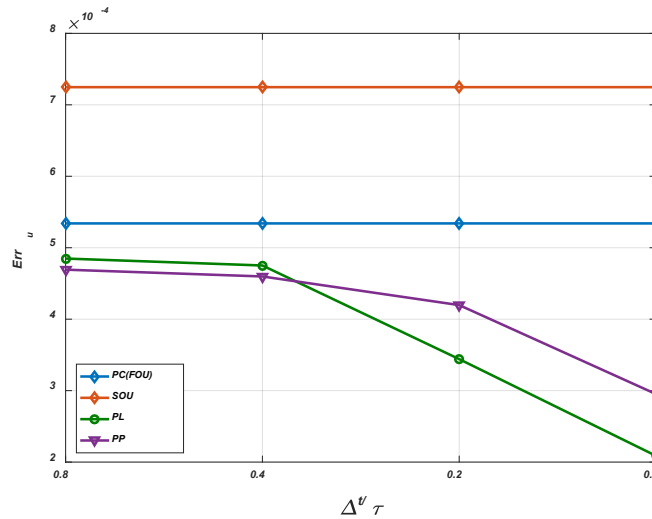

Figure 13. The velocity errors of Couette flow at different temporal resolutions for different Godunov-type and non-Godunov flux schemes

6.3 Pressure-driven Poiseuille flow

This flow has its analytical velocity and pressure defined as:

$$u_a = \frac{1}{2\mu}\left(\frac{dp}{dx}\right)\left[y(y - D_y)\right] \tag{75}$$

$$p_a = p_{in} + \left(\frac{dp}{dx}\right)x \tag{76}$$

where μ is the dynamic viscosity, D_y is the height of the flow channel, and p_{in} is the inlet pressure. After defining different pressures at the inlet and outlet, dp/dx can be expressed as:

$$\left(\frac{dp}{dx}\right) = \frac{p_{out} - p_{in}}{D_x} \tag{77}$$

The maximum velocity appears at $D_y/2$, so:

$$u_{a,max} = -\frac{1}{8\mu}\left(\frac{p_{out} - p_{in}}{D_x}\right)D_y^2 \tag{78}$$

By carefully choosing the values for p_{in} and p_{out}, the Mach number is kept *Ma*=0.01 again in the current study by using $u_{a,max}$ as the characteristic velocity. For the study of flux schemes at different mesh resolutions, $\tau = 0.006$ and $\Delta t = 0.4\tau$. The same set of IRT meshes is used for the study. The errors in

velocity and density of different Godunov-type flux schemes at different mesh resolutions are shown in Fig. 14 and Fig. 15, in which the pressure and density are related by:
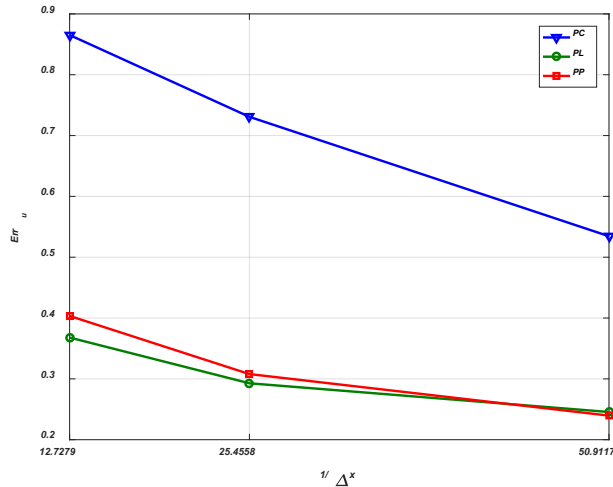
$$p = c_s^2 \rho \tag{79}$$

Figure 14. The velocity errors of Poiseuille flow at different mesh resolutions for different Godunov-type flux schemes

In Fig. 14, it can be observed that the PL and PP schemes generate much less error than the PC scheme at all mesh resolutions. This is because, like the TGV flow, the solution of Poiseuille flow is also viscosity-dependent. High-order schemes such as PL and PP can generate much less numerical viscosity than the PC scheme. By comparing PL and PP, a similar observation to the Couette flow can be made, which is that the pivotal mesh resolution for the PP scheme to generate more accurate results than the PL scheme is within the tested range.

Similarly, Fig. 15 shows the density errors. The PL scheme produces smaller errors than the PC scheme at all mesh resolutions. However, the PP scheme is even less accurate than the PC scheme, which is the opposite of the velocity error in Fig. 14. In kinetic theory, velocity is a higher-order moment than density. Therefore, the velocity solution can benefit from the usage of higher-order spatial discretization schemes, which may not improve the solution accuracy in density.
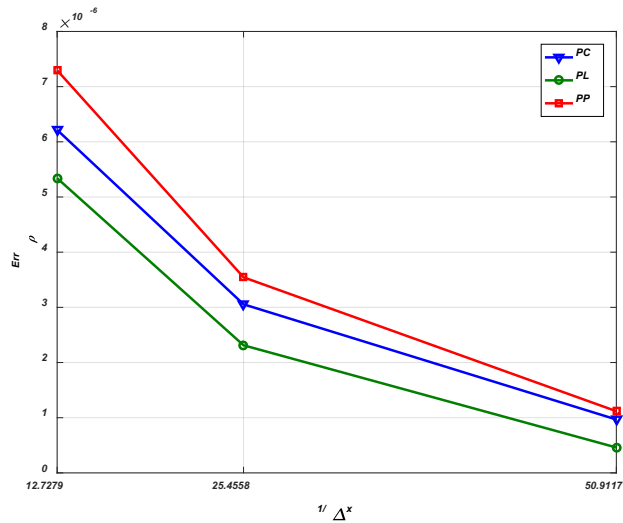
Figure 15. The density errors of Poiseuille flow at different mesh resolutions for different Godunov-type flux schemes
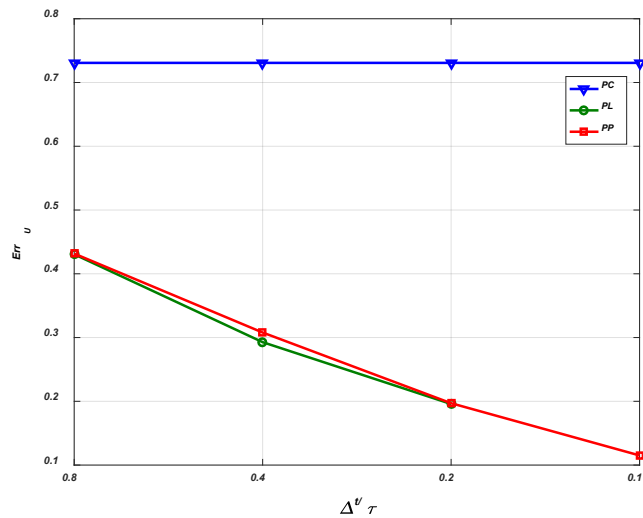

Figure 16. The velocity errors of Poiseuille flow at different temporal resolutions for different Godunov-type flux schemes

The effect of the temporal resolutions on the spatial errors is also studied for Poiseuille flow. The same 36*36 IRT mesh is applied. Figures 16 and 17 show the velocity errors and density errors, respectively. Like Couette flow, two common conclusions can be drawn. First, the PC(FOU) scheme is Δt-independent. Second, the PL and PP schemes can monotonically decrease the error, both in velocity and density, while increasing the temporal resolution. However, it is worth noting that the PL scheme does not have data points at $\Delta t/\tau = 0.1$ in both Fig. 16 and 17. This is because at such a small Δt, the PL scheme becomes unstable. Fortunately, the PP scheme is able to obtain a stable and accurate result at such small temporal resolution.
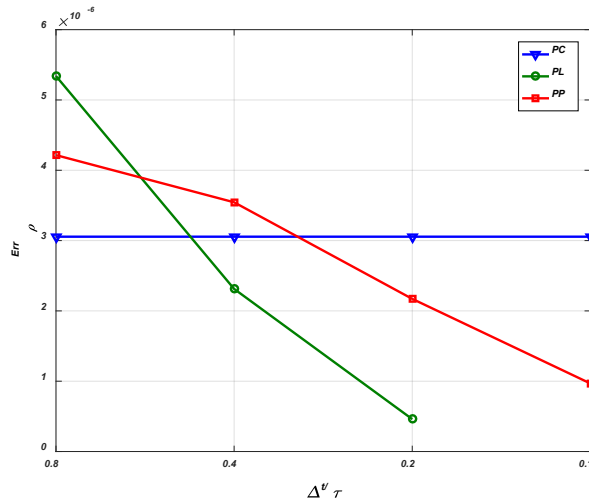
Figure 17. The density errors of Poiseuille flow at different temporal resolutions for different Godunov-type flux schemes

6.4 Flow past a circular cylinder at Re=20

The last simulation case is the flow over a circular cylinder in order to test the developed Godunov- type flux schemes on the general unstructured mesh (Fig. 9(b)). The geometric configuration of the computational domain and the generated mesh are shown in Fig. 18, in which D is the diameter of the cylinder.
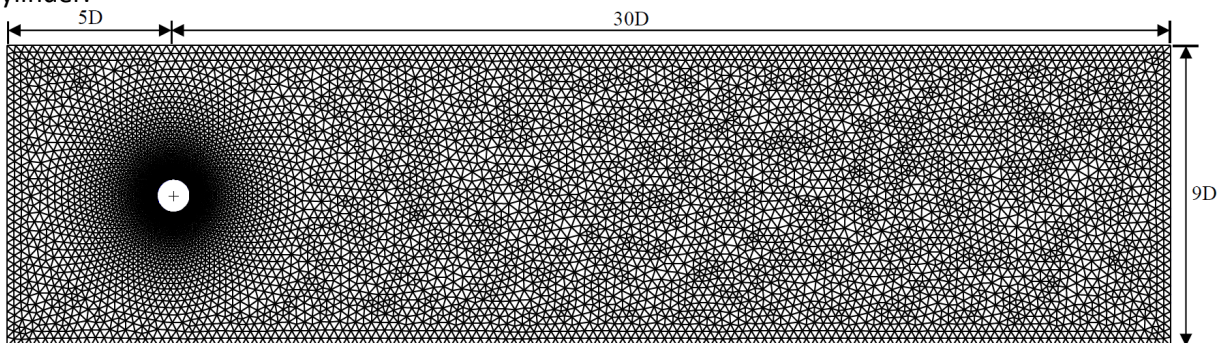

Figure 18. The geometry and unstructured triangular mesh of the flow over a circular cylinder

The physical boundary conditions for each boundary are defined as follows. The left boundary, which is the inlet of the flow, is defined with a uniform x-velocity and zero y-velocity. The outlet on the right is considered a fully-developed boundary. The surface on the circular cylinder is an immersed boundary with the nonslip condition, in which both the x- and y-velocities are zero. The top and bottom surfaces are periodic. A D2Q9 lattice is applied for the simulation. The Reynolds number of the flow is kept at *Re*=20 by choosing *Ma*=0.11574. First, all three flux schemes are tested at $\Delta t/\tau = 0.2$. Then, an attempt to improve the accuracy by decreasing Δt is made. After several trials, the smallest Δt to maintain a stable solution for the PP scheme is obtained, in which $\Delta t/\tau = 0.1648$. However, at such a temporal resolution, the PL scheme becomes unstable. The streamlines around the circular cylinder at steady state for the PC, PL, and PP schemes at $\Delta t/\tau = 0.2$ and the PP scheme at $\Delta t/\tau = 0.1648$ are shown in Fig. 19. Their vortex length ratio (L/a), separation angle (θ_S) and drag coefficient (C_D) along with some published data are listed in Tab. 1.
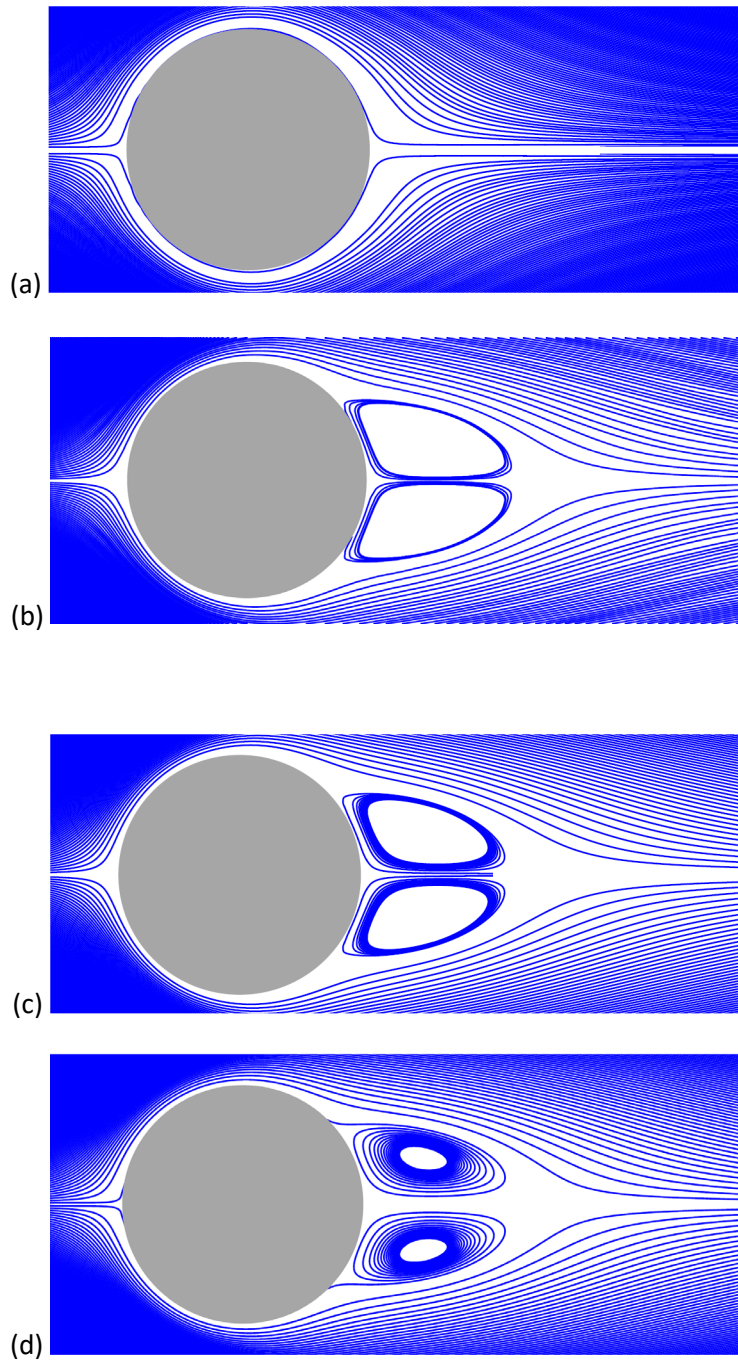
Figure 19. Vortex structures behind the circular cylinder with different Godunov-type flux schemes and temporal resolutions at Re=20. (a) PC at $\Delta t/\tau = 0.2$; (b) PL at $\Delta t/\tau = 0.2$; (c) PP at $\Delta t/\tau = 0.2$; (d) PP at $\Delta t/\tau = 0.165$

First, it can be seen that the PC scheme is so diffusive that no vortices developed behind the cylinder. Further, by comparing the detailed values in Tab. 1, it can be observed that at the same spatial and temporal resolution, the PP scheme is slightly more accurate than the PL scheme. For the PP scheme, by decreasing Δt, the accuracy can be further improved, which is consistent with the Couette flow and

Poiseuille flow studies. Continuing to decrease Δt will make the PP scheme unstable as well. However, although the numerical solutions are reasonably close to the benchmark data for validation of these schemes, there is still room for further improvement in future work. As discussed in Sec. 3.1, the replacement of first-order interpolation, Eq. (26), with a higher-order scheme can further improve the accuracy, but since the interpolation scheme is a separate topic from the flux schemes, the effects on the accuracy from testing different interpolations are not included here.

		L/a	θ_s	C_D
Coutanceau and Bouard [43]		1.860	44.80	-
Dennis and Chang [44]		1.880	43.70	2.045
Nieuwstadt and Keller [45]		1.786	43.37	2.053
Fornberg [46]		1.820	-	2.000
Calhoun [47]		1.820	-	2.190
Ye et al. [48]		1.840	-	2.030
He and Doolen [49]		1.842	42.96	2.152
Mei and Shyy [40]		1.804	-	-
Lee and Lin [50]		1.834	-	2.106
Ubertini et al. [7]		-	-	2.090
Zarghami et al. [9]		1.820	42.50	2.205
Patil and Lakshmisha [19]		1.884	42.81	1.949
Present	**PC at $\Delta t/\tau = 0.2$**	**0**	**0**	**4.1723**
	PL at $\Delta t/\tau = 0.2$	**1.5897**	**43.9683**	**2.7481**
	PP at $\Delta t/\tau = 0.2$	**1.5953**	**44.3451**	**2.625**
	PP at $\Delta t/\tau = 0.165$	**1.6353**	**44.9915**	**2.6104**

Table 1. Comparison of geometrical and dynamical parameters with different Godunov-type flux schemes and temporal resolutions for flow past a circular cylinder at Re=20

7. Conclusions

In the current work, a systematic approach to developing Godunov-type flux schemes that do not need Riemann solvers for the FVDBM on a triangular unstructured mesh is proposed. With the PC, PL, and PP wave reconstructions, three Godunov-type flux schemes with increasing theoretical orders of accuracy are formulated. Additionally, the SOU flux scheme, which is non-Godunov, is provided for comparison. After testing these flux schemes on different problems with different boundary conditions, different solution features, and different mesh topologies, four common conclusions can be made. First, due to the wave-like treatment of the PDF advection, the Godunov-type PL flux scheme presents better spatial accuracy than its non-Godunov counterpart, the SOU (the PP is also better than the SOU, but they have different orders of accuracy). Second, the PL and PP scheme are much more accurate than the PC scheme in terms of velocity solutions; third, the PP scheme is only more accurate than the PL scheme when the mesh resolution is above a certain value; fourth, for the PL and PP scheme, increasing the temporal resolution can increase the spatial accuracy, while the spatial accuracies of FOU and SOU are not affected by the temporal resolution. However, such an increase of temporal resolution is limited by a stability condition. As a result, it is recommended to use the PL scheme at low or moderate spatial resolution while choosing the PP scheme for the problems that require a high level of accuracy and extreme fine mesh.

8. Acknowledgements

References

[1] S. Succi, G. Amati, R. Benzi. Challenges in lattice Boltzmann computing. Journal of statistical physics. 81, 5(1995).

[2] T. Abe. Derivation of the lattice Boltzmann method by means of the discrete ordinate method for the Boltzmann equation. Journal of computational physics. 131, 241(1997).

[3] N. Cao, S. Chen, S. Jin, D. Martinez. Physical symmetry and lattice symmetry in the lattice Boltzmann method. Physical review E. 55, R21(1997).

[4] X. He, L. Luo. Theory of the lattice Boltzmann method: From the Boltzmann equation to the lattice Boltzmann equation. Physical review E. 56, 6811(1997).

[5] X. He, L. Luo. A priori derivation of the lattice Boltzmann equation. Physical review E. 55, R6333(1997).

[6] S. Ubertini, G. Bella, S. Succi. Lattice Boltzmann method on unstructured grids: Further developments. Physical review E. 68, 016701(2003).

[7] S. Ubertini, S. Succi, G. Bella. Lattice Boltzmann schemes without cordinates. Philosophical transactions of the royal society of London-Mathematical, Physical, and Engineering Sciences 362, 1763(2004).

[8] N. Rossi, S. Ubertini, G. Bella and S. Succi. Unstructured lattice Boltzmann method in three dimensions. International journal for numerical methods in fluids. 49, 619(2005).

[9] A. Zarghami, M. Maghrebi, J. Ghasemi and S. Ubertini. Lattice Boltzmann finite volume formulation with improved stability. Communications in Computational Physics. 12, 42(2012).

[10] A. Zarghami, S. Ubertini and S. Succi. Finite-volume lattice Boltzmann modeling of thermal transport in nanofluids. Computers & Fluids. 77, 56(2013).

[11] A. Zarghami, C. Biscarini, S. Succi and.S. Ubertini Hydrodynamics in porous media: A finite volume lattice Boltzmann study. Journal of Scientific Computing. 59, 80(2014).

[12] G. Peng, H. Xi, C. Duncan. Lattice Boltzmann method on irregular meshes. Physical review E. 58, R4124(1998).

[13] H. Xi, G. Peng, S. Chou. Finite-volume lattice Boltzmann method. Physical review E. 59, 6202(1999).

[14] G. Peng, H. Xi, C. Duncan. Finite volume scheme for the lattice Boltzmann method on unstructured meshes. Physical review E. 59, 4675(1999).

[15] H. Xi, G. Peng, S. Chou. Finite-volume lattice Boltzmann schemes in two and three dimensions. Physical review E. 60, 3380(1999).

[16] G. Peng, H. Xi, and S. Chou. On Boundary Conditions in The Finite Volume Lattice Boltzmann Method On Unstructured Meshes. International journal of modern physics C. 10, 1003(1999).

[17] J. Ghasemi, S. E. Razavi. On the finite-volume lattice Boltzmann modeling of thermo-hydrodynamics. Computers and mathematics with applications. 60, 1135(2010).

[18] M. Stiebler, J. Tölke, M. Krafczyk. An upwind discretization scheme for the finite volume lattice Boltzmann method. Computers & Fluids. 35, 814(2006).

[19] D. V. Patil, K. N. Lakshmisha. Finite volume TVD formulation of lattice Boltzmann simulation on unstructured mesh. Journal of computational physics. 228, 5262(2009).

[20] D. V. Patil, K. N. Lakshmisha. Two-dimensional flow past circular cylinders using finite volume lattice Boltzmann formulations. International journal for numerical methods in fluids. 69, 1149(2012).

[21] D. V. Patil. Chapman-Enskog analysis for finite-volume formulation of lattice Boltzmann equation. Physica A. 392, 2701(2013).

[22] S. K. Choi and C. L. Lin. A simple finite-volume formulation of the lattice Boltzmann method for laminar and turbulent flows. Numerical Heat Transfer, Part B. 58, 242(2010).

[23] D Yu, R. Mei, L. Luo and W. Shyy. Viscous flow computations with the method of lattice Boltzmann equation. Progress in Aerospace Sciences. 39, 329(2003).

[24] R. Zhang, H. Fan and H. Chen. A Lattice Boltzmann approach for solving scalar transport equations. Philosophical Transactions of The Royal Society A. 369, 2264(2011).

[25] L. Chen and L. Schaefer. A unified and preserved Dirichlet boundary treatment for the cell-centered finite volume discrete Boltzmann method. Physics of Fluids. 27, 027104(2015).

[26] X. Shan, X. Yuan and H. Chen. Kinetic theory representation of hydrodynamics: a way beyond the Navier-Stokes equation. Journal of Fluid Mechanics. 550, 413(2006).

[27] P. L. Roe. Approximate Riemann solvers, parameter vectors, and difference scheme. Journal of Computational Physics. 43, 357(1981).

[28] S. K. Godunov. A finite-difference method for the numerical computation and discontinuous solutions of the equations of fluid dynamics. Mathematics of the USSR-Sbornik. 47, 271(1959).

[29] B. van Leer. Towards the ultimate conservative difference scheme. I. The quest of monotonicity. Lecture Notes in Physics. 18, 163(1973).

[30] B. van Leer. Towards the ultimate conservative difference scheme. II. Monotonicity and conservation combined in a second-order scheme. Journal of Computational Physics. 14, 361(1974).

[31] B. van Leer. Towards the ultimate conservative difference scheme. III. Upstream-centered finite-difference schemes for ideal compressible flow. Journal of Computational Physics. 23, 263(1977).

[32] B. van Leer. Towards the ultimate conservative difference scheme. IV. A new approach to numerical convection. Journal of Computational Physics. 23, 276(1977).

[33] B. van Leer. Towards the ultimate conservative difference scheme. V. A second-order sequel to Godunov's method. Journal of Computational Physics. 32, 101(1979).

[34] P. Colella. A direct Eulerian MUSCL scheme for gas dynamics. SIAM Journal on Scientific and Statistical Computing. 6, 104(1985).

[35] P. Colella and P. R. Woodward. The Piecewise parabolic method (PPM) for gas-dynamical simulations. Journal of Computational Physics. 54, 174(1984).

[36] S. Teng, Y. Chen and H. Ohashi. Lattice Boltzmann simulation of multiphase fluid flows through the total variation diminishing with artificial compression scheme. International Journal of Heat and Fluid Flow. 21, 112(2000).

[37] T. Lee, C. Lin and L. Chen. A lattice Boltzmann algorithm for calculation of the laminar jet diffusion flame. Journal of Computational Physics. 215, 133(2005).

[38] J. B. Goodman and R. J. LeVeque. On the accuracy of stable schemes for 2D scalar conservation laws. Mathematics of Computation. 45, 171 (1985).

[39] P. L. Bhatnagar, E. P. Gross,t and M. Krook. A Model for Collision Processes in Gases. I. Small Amplitude Processes in Charged and Neutral One-Component System. Physical review. 94, 511(1954).

[40] R. Mei and W. Shyy. On the Finite Difference-Based Lattice Boltzmann Method in Curvilinear Coordinates. Journal of Computational Physics. 143, 426(1998).

[41] Randall J. Leveque. Finite Volume Methods for Hyperbolic Problems. Cambridge University Press. 2002, pp. 66.

[42] Z. Guo, C. Zheng, B. Shi. Non-equilibrium extrapolation method for velocity and pressure boundary conditions in the lattice Boltzmann method. Chinese Physics. 11, 366(2002).

[43] M. Coutanceau and R. Bouard. Experimental determination of the main features of the viscous flow in the wake of a circular cylinder in uniform translation: part 1: steady flow, part 2: unsteady flow. Journal of Fluid Mechanics, 79 (1977), 231.

[44] S. C. R. Dennis and G. Z. Chang. Numerical solutions for steady flow past a circular cylinder at Reynolds numbers up to 100. Journal of Fluid Mechanics. 42 (1970), 471.

[45] F. Nieuwstadt and H. B. Keller. Viscous flow past circular cylinders. Computers & Fluids. 1 (1973), 59.

[46] B. Fornberg. A numerical study of steady viscous flow past a circular cylinder. Journal of Fluid Mechanics. 98 (1980), 819.

[47] D. Calhoun. A Cartesian grid method for solving the two-dimensional streamfunction-vorticity equations in irregular regions. Journal of Computational Physics. 176 (2002), 231.

[48] T. Ye, R. Mittal, H. S. Udaykumar and W. Shyy. An accurate Cartesian grid method for viscous incompressible flows with complex immersed boundaries. Journal of Computational Physics. 156 (1999), 209.

[49] X. He, G. Doolen. Lattice Boltzmann Method on Curvilinear Coordinates System: Flow around a Circular Cylinder. Journal of Computational Physics. 134, 306(1997).

[50] T. Lee, C. Lin. An Eulerian description of the streaming process in the lattice Boltzmann equation. Journal of computational physics. 185, 445(2003).